Curvature Dynamics of PEGDA Asymmetric Networks via Frontal Photopolymerization: Effect of Chain Length and Optical Attenuation

Macromolecules

pubs.acs.org/Macromolecules
Article

Curvature Dynamics of PEGDA Asymmetric Networks via Frontal Photopolymerization: Effect of Chain Length and Optical Attenuation

Muhammad Ghifari Ridwan, Huseyin Mirac Dizman, Isobel Bentley, Alessandra Vitale, and João T. Cabral*

Cite This: *Macromolecules* 2026, 59, 1978−1986

ABSTRACT: We investigate how the oligomer molecular mass, chain length, and optical attenuation affect both polymerization kinetics and the spatiotemporal response of materials patterned via frontal photopolymerization (FPP). We employ model poly(ethylene glycol) diacrylate (PEGDA) oligomers of different chain lengths and investigate their FPP kinetics and response following solvent development, focusing on the emergence and evolution of the material curvature. We find that longer precursors yield a lower dose (or time) threshold for solidification, effectively benefiting from an "early start," while the front velocity remains unchanged with chain length; by contrast, photoinitiator concentration leads to a nonmonotonic impact on kinetics due to the combined effects on rate and optical attenuation, which we collapse on a master curve. FPP networks can exhibit nonmonotonic, spontaneous curvature fluctuations, from flat or convex, to concave, and back to convex, that we show to depend on PEGDA chain length and describe by a minimal evaporation−diffusion model. These findings demonstrate how the interplay between molecular structure, soft mechanics, and solvent transport can be harnessed to program the response of asymmetric polymer networks.

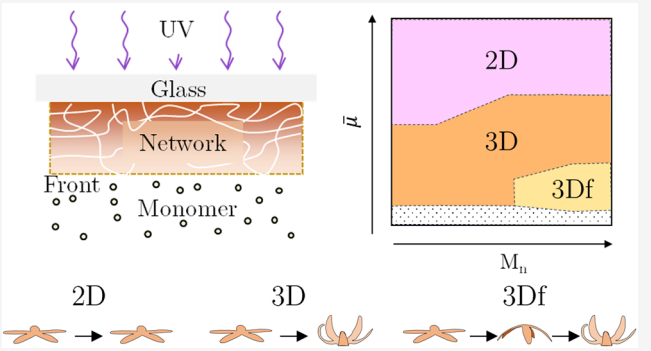

INTRODUCTION

Concepts for 4D soft materials, systems that change shape or function over time with or without external stimuli, have developed rapidly over the past decade in polymer science.[1−4] By contrast with conventional static polymers or network structures, 4D materials are programmed during fabrication to evolve predictably under environmental changes such as temperature,[5] moisture,[6] pH,[7] light,[8] or solvent swelling/deswelling.[9] These transformations are driven by a symmetry-breaking property, for instance, an asymmetry in material architecture or physicochemistry, that results in autonomous, reversible, and stimulus-responsive behavior. Emergent phenomena in connected functional units have been demonstrated in a range contexts, where interactions lead to complex and often unexpected response.[10−12] Such approaches unlock a range of possibilities for nonplanar material assembly and origami, where complex 3D shapes or motion arise from controlled deformation of initially flat or simple geometries.[5,13,14]

One powerful strategy for achieving such transformations in polymer networks is by engineering internal gradients throughout the material, such as variations in cross-link density, stiffness, swelling capacity, or residual stresses. These gradients induce nonuniform deformation upon stimulation, resulting in bending,[9] twisting,[15,16] folding,[9,14] or buckling.[17] Unlike mechanical actuators or multimaterial composites, such materials can encode "instructions" for shape change at the molecular level during synthesis. As a result, gradient-based 4D materials offer a scalable and elegant route to construct shape-shifting structures, ranging from soft robotics,[18] sensors,[19] and bioinspired devices.[20]

Frontal photopolymerization (FPP) is a versatile approach for creating asymmetric polymeric networks with exceptional control of the conversion both along the direction of illumination (z) and within the plane (xy), by employing a photomask or modulated illumination.[21−23] In FPP, light initiates a planar polymerization front that travels through a liquid monomer or prepolymer, under conditions of strong light attenuation and limited mass and thermal diffusion conditions, converting it into polymer network.[24] This process

Received: October 8, 2025
Revised: January 26, 2026
Accepted: January 29, 2026
Published: February 12, 2026

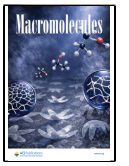

https://doi.org/10.1021/acs.macromol.5c02783
Macromolecules 2026, 59, 1978−1986

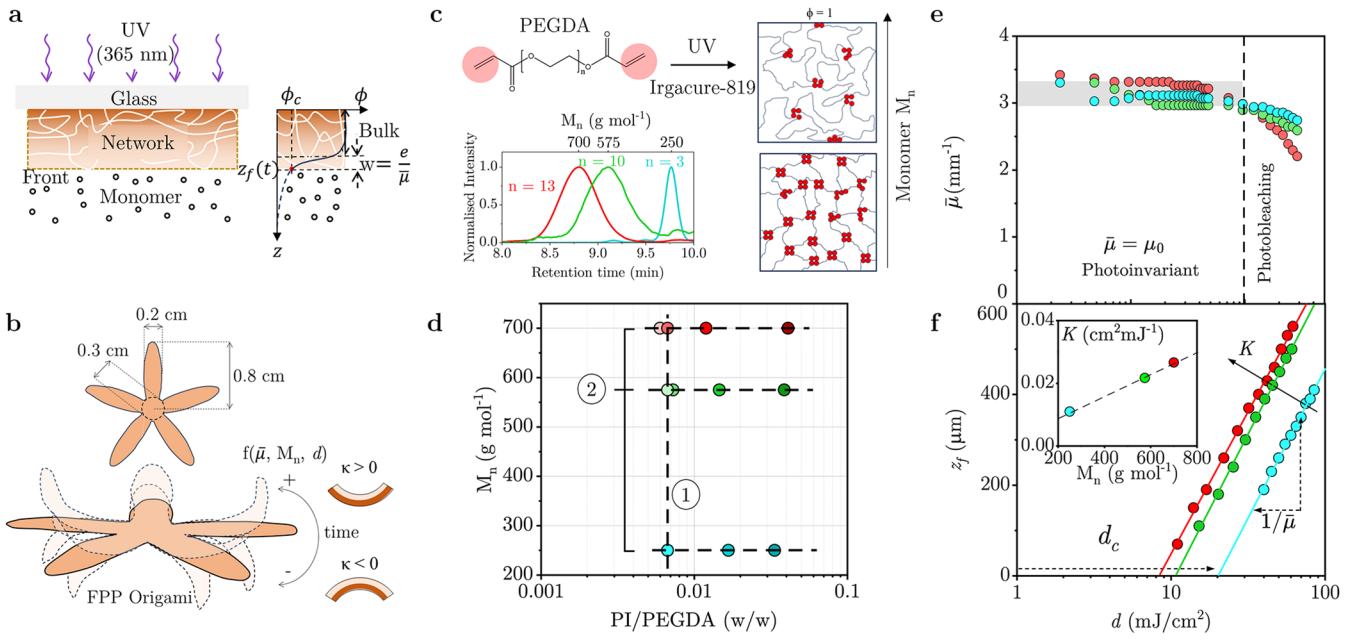

Figure 1. (a) FPP schematic depicting the frontal network formation, accompanied by a sharp conversion profile $\phi(z)$, with front position z_f corresponding to the intersection with a critical conversion value $\phi = \phi_c$, yielding an interfacial width w governed by optical attenuation coefficient $\bar{\mu}$. (b) Nonplanar material design (illustrated with a "starfish" pattern) and schematic of dynamic response governed by oligomer molecular mass (M_n), optical attenuation $\bar{\mu}$, and irradiation dose d. Curvature κ is defined in terms of the network asymmetry, $\kappa > 0$ if it curves toward less cross-linked interface, and $\kappa < 0$ if toward the illuminated surface. (c) Chemical structure of the PEGDA oligomer and size distribution obtained by GPC for PEGDA with M_n of 250 (blue), 575 (green), and 700 (red) g mol^{-1} corresponding to 3, 10, and 13 ethylene glycol (EG) repeat units. Schematic of network formation for low and high M_n at full conversion $\phi \equiv 1$. (d) Experimental map of PI/PEGDA (w/w) ratio at varying M_n, defining representative isopleths ① and ②. The gradient of color intensity corresponds to the PI fraction. (e) Evolution of optical attenuation coefficient $\bar{\mu}$ with irradiance dose d, where the vertical dashed line indicates conditions up to which the process is effectively photoinvariant ($\bar{\mu} \approx \mu_0$). Data for M_n 700 g mol^{-1} have been previously reported[33] and are included here for comparison. (f) Logarithmic growth of front position, z_f, with irradiation dose, d, with a proportionality constant of $1/\bar{\mu}$ and an x-axis intersection at the critical irradiation dose d_c, as described by eq 2. The inset shows that the effective FPP conversion constant K increases linearly with PEGDA M_n.

inherently generates spatial gradients in polymer conversion, leading to variations in cross-linking density and stiffness along the front's propagation direction.[22] Material gradients arise from differences in exposure time, heat generation, system chemical composition, radical diffusion, and polymerization kinetics. Unlike layer-by-layer methods, FPP enables single-step fabrication of morphologically dynamic materials with built-in structural heterogeneity.[9,13]

The cross-sectional profile of the traveling waves of network formation can be effectively tuned by adjusting formulation parameters and front propagation conditions,[23,25,26] and under a range of practically relevant conditions, profiles are shape-invariant and exhibit predictive propagation kinetics, yielding well-defined asymmetric networks of prescribed dimensions. When exposed to an external stimulus, such as solvent swelling/deswelling, these networks undergo predictable deformation into complex nonplanar shapes.[5,9,13,27,28] This curvature-inducing behavior is central to many natural systems, from plant movement to tissue morphogenesis,[29−31] and is increasingly being replicated in synthetic materials.[32]

In this paper, we investigate the effect of the chain length of the precursor oligomer, employed as a "photoresist," on the resulting asymmetric properties and stimuli-responsive behavior of 4D FPP networks. Our hypothesis is that the mass of a model difunctional oligomer can be an effective design parameter of gradient networks with prescribed mesh size and thus soft mechanics and transport properties.[34] Understanding how chain length affects not only FPP kinetics but also the distribution of internal stresses and curvature evolution during solvent swelling and drying is essential for designing materials with a predictable 4D behavior. We select a difunctional acrylate oligomer, poly(ethylene glycol) diacrylate or PEGDA, as a model system, as it can form networks and hydrogels with a range of practical biomedical, sensing, and separation applications. We examine the role of PEGDA chain length, optical attenuation, and photoinitiator stoichiometry in FPP kinetics and 4D response of asymmetric networks following solvent development. We demonstrate that oligomer chain length provides an effective lever to not only tune FPP propagation but also to selectively control the spatiotemporal response and nonplanar assembly of otherwise identical asymmetric FPP networks. We then introduce a minimal model that combines FPP kinetics with evaporation−diffusion of the solvent that can capture our experimental observations of emerging curvature and curvature fluctuations and thus provide a framework for the design of 4D materials based on structurally encoded gradients.

EXPERIMENTAL SECTION

To fabricate asymmetric polymer networks with different molecular mesh sizes, poly(ethylene glycol) diacrylate (PEGDA) with three different number-average molecular masses (M_n) of 250, 575, and 700 g mol^{-1} (Sigma-Aldrich, references 475629, 437441, 455008) and photoinitiator (PI) phenylbis(2,4,6-trimethylbenzoyl)phosphine oxide (Irgacure-819, BASF, 30128871) were used. PI/PEGDA ratios ranging from 0.0005 to 0.07 w/w (defined as mass of PI over mass of PEGDA) were investigated (defined as mass of PI over mass of PEGDA). Batches of 15 g of PEGDA precursor and PI were mixed

https://doi.org/10.1021/acs.macromol.5c02783
Macromolecules 2026, 59, 1978−1986

using a magnetic stirrer at 750 rpm for 1 h and subsequently wrapped with aluminum foil and stored at 4 °C to prevent inadvertent polymerization. Ethanol (VWR Chemicals 99.97%, code 20821.321) was used for development (by solvent immersion) without further purification.

A collimated UV light source (Omnicure S1500, equipped with a 365 nm filter) was employed, and a VItec RS-365 digital radiometer (Spectroline) was employed to calibrate and measure irradiance, generally fixed between 2 and 2.5 mW/cm^2. The PEGDA/PI mixture (~0.625 mL) was placed between two microscope glass slides (1 × 3 in., Fisherbrand 1238−3118) separated by 1−3 mm spacers. Photomasks were designed using AutoCAD (2024) and printed onto the acetate film using a laser printer at 600 dpi resolution, and placed atop the upper glass slide. After exposure, the printed polymeric network (~0.02 mL) was pad dried, and its thickness was measured using a digital caliper (Mitutoyo, model PK-0505CPX). The sample was then developed by immersion in ethanol (typically 10 mL). The resulting structures were imaged using a BASLER acA640-750uc camera fitted with a 0.5−1X Edmund Optics lens (87535).

RESULTS AND DISCUSSION

We first consider the kinetics of network formation by frontal photopolymerization (FPP), depicted in Figure 1a. Upon UV light irradiation, a polymerization front propagates through the resin, forming a well-defined boundary that separates the unreacted precursor from the cross-linked network. After removal of excess liquid PEGDA and pad drying, the position of the front z_f along the illuminated axis (z) defines the network thickness for a given irradiation dose d.[21,24] The resulting network has an asymmetric cross-section described by an order parameter $\phi(z)$, defined between 0 and 1, corresponding to neat precursor and full conversion, respectively. The illuminated surface exhibits a greater ϕ, which decreases toward the network−liquid interface, where $\phi \equiv \phi_c$, a system-specific threshold value for network formation. The sigmoidal $\phi(z)$ profile, defined by an interfacial width w, propagates during photopolymerization as a planar wave, with a shape-invariant profile in many practically relevant conditions.[25,35]

Figure 1b depicts a starfish-shaped pattern (xy) and possible spatiotemporal responses for asymmetric networks, namely, the emergence of curvature κ toward the illuminated surface ($\kappa < 0$) or toward the network−liquid interface ($\kappa > 0$), which we hypothesize to be a function of the optical properties, precursor molecular mass, and irradiance. This "starfish" illustrative geometry enables a visualization of network response to molecular and FPP parameters and development. We select PEGDA of three different number-average molecular masses (M_n) 250, 575, and 700 g mol^{-1} which are liquid at room temperature, with ethylene glycol repeating units n = 3, 10, and 13, respectively (Figure 1c). Higher M_n (≥1000 g mol^{-1}) correspond to PEGDA that are solid at room temperature and thus not suited as liquid FPP photoresists. An illustration of fully converted ($\phi = 1$) networks architecture of high and low precursor M_n is also provided.

FPP Coarse-Grained Model

To interpret our experimental results, we employ a well established coarse-grained analytical model describing the kinetics of FPP.[21−26,36,37] The simplest, minimal model is based on a typical first-order reaction equation of normalized monomer-to-polymer conversion ϕ, and a differential Beer−Lambert law to capture the directional light attenuation of the medium during photoconversion. As the directional solidification progresses, conversion may induce changes in light attenuation, which is modeled as a composition-average optical attenuation coefficient, $\bar{\mu}(z, t) = \mu_0(1 - \phi(z, t)) + \mu_\infty\phi(z, t)$, where μ_0 is the coefficient of the neat resin and μ_∞ is the coefficient of the fully converted material. While in general $\bar{\mu}$ evolves over the course of the reaction, in the case of photoinvariant systems (or regimes), $\bar{\mu} \approx \mu_0$. An analytical expression for the normalized conversion profile along the solidification direction (z-axis) is then obtained

$$\phi(z, d) = 1 - \exp[-Kd\exp(-\bar{\mu}z)] \quad (1)$$

By defining the normalized critical monomer-to-polymer conversion ϕ_c as the value of ϕ at the front position z_f (corresponding to the polymer thickness), we obtain

$$z_f(d) = \frac{\ln[Kd/\ln(1/(1-\phi_c))]}{\bar{\mu}} \quad (2)$$

where K characterizes the FPP kinetics. The critical (or lowest) irradiation dose d_c, required for ϕ to first reach ϕ_c and thus $z_f > 0$, is obtained by rearranging eq 2, yielding $d_c = \frac{1}{K}\ln\frac{1}{1-\phi_c}$. The interfacial width can be defined as $w \equiv e/\bar{\mu}$, characterizing the conversion gradient of the resulting asymmetric network.

Effect of PEGDA Molecular Mass on FPP Kinetics

We investigated experimentally the influence of the molecular mass of the PEGDA precursor on FPP kinetics. Three PEGDA lengths are selected, with number-average molecular mass, namely, M_n = 250, 575, and 700 g mol^{-1}, while maintaining a constant PI-to-PEGDA ratio (w/w) of 0.67% (corresponding to isopleth line ① in Figure 1d). Fourier transform infrared (FTIR) spectroscopy measurements (SI Section S1) were employed to determine the critical conversion ϕ_c, which was found to be approximately the same across all three precursor PEGDA molecular masses ($\phi_c \approx 0.2$). To validate the applicability of the photoinvariant FPP model to this investigated system, the attenuation coefficient μ was measured under continuous UV irradiation. A constant value of μ was observed for irradiation doses below 700 mJ/cm^2, which thus provides an upper bound for the photoinvariant regime (Figure 1e). Beyond this dose, photobleaching takes place and μ decreases with further exposure.

We characterize FPP front propagation kinetics by fabricating networks at varying irradiation doses d and measuring the resulting solid−liquid front position z_f. Within the coarse-grained FPP framework,[21] it follows from eq 2 that the inverse slope and the z_f-intercept of a semilogarithmic plot of z_f vs d yield $\bar{\mu}$ and the critical irradiation dose d_c, respectively. Experimental data show invariant slopes for all M_n in Figure 1f, indicating that $\bar{\mu}$ remains constant, with an average value of 3.4 ± 0.2 mm^{-1}. This is expected, as the PI is the dominant absorbing species, and its concentration is constant across all three formulations, fixed at 0.0067 w/w, corresponding to 0.67% w/w PI/PEGDA. However, the z_f-axis intercepts for three different M_n are clearly distinct, yielding different critical doses, namely, d_c = 21.3, 9.2, and 7.6 mJ/cm^2, for M_n = 250, 575, 700 g mol^{-1}, respectively. Higher M_n thus leads to a lower d_c (Figure 1f) or, equivalently, a lower induction time for solidification. Knowing ϕ_c and eq 2, we calculate the effective rate constant K for each oligomer based on Figure 1f: 0.011, 0.022, and 0.027 cm^2 mJ^{-1} for M_n = 250, 575, and 700 g mol^{-1}, respectively, following that higher M_n also leads to a higher front propagation rate, K. Interestingly, the velocity of FPP wave propagation is not well-defined as it

https://doi.org/10.1021/acs.macromol.5c02783
Macromolecules 2026, 59, 1978−1986

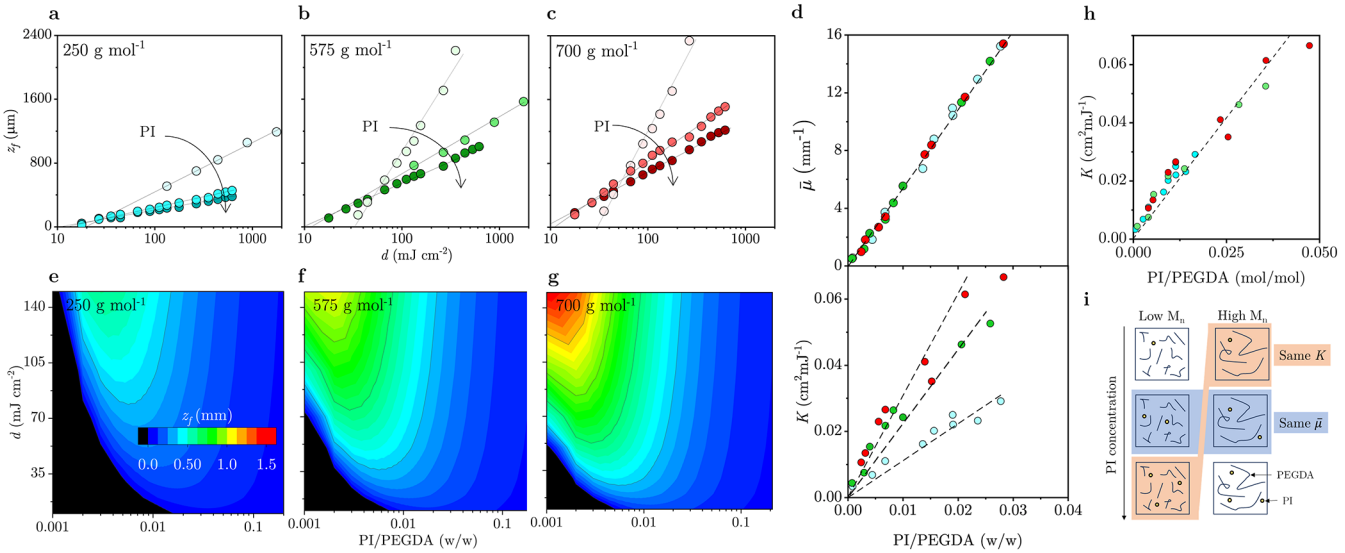

Figure 2. FPP kinetics measured in terms of front position z_f and irradiation dose d (mJ cm^{-2}) and increasing photoinitiator concentration for (a) PEGDA M_n = 250 g mol^{-1}, (b) 575 g mol^{-1} and (c) 700 g mol^{-1}, corresponding to isopleth ② in Figure 1d. Lines are logarithmic fits to eq 2 yielding $\bar{\mu}$ and K. (d) Optical attenuation coefficient $\bar{\mu}$ increases linearly with PI/PEGDA (w/w) and collapses for all M_n, while the FPP kinetics constant K increases with M_n. (e–g) Heat map of z_f for different irradiation doses and PI:PEGDA ratios (w/w) for PEGDA M_n 250, 575, and 700 g mol^{-1}. (h) Constant K effectively collapses for all M_n and constant PI:PEGDA stoichiometric ratio. (i) Illustration of the combined effects of PEGDA M_n and PI, including conditions for constant K at identical PI/PEGDA stoichiometric ratio, and constant $\bar{\mu}$ at fixed PI concentration.

varies over time (or z). We find that the traveling wave velocity is effectively constant for all M_n investigated, at constant d, and that the role of the precursor molecule M_n is simply that of changing d_c. In simple terms, higher M_n benefit from an "earlier start" associated with their lower d_c. At constant illumination dose (or time), networks originating from higher M_n thus grow taller, as the overall process is more "efficient." We elaborate on these observations in SI Section S2, rationalized in terms of our minimal model.

Nonmonotonic Dependence of FPP Kinetics on Photoinitiator Concentration

We next quantify the impact of the PI concentration on FPP kinetics for PEGDA oligomers of different M_n. For this analysis, we select a series of PI:PEGDA (w/w), R_w, to maintain constant PI:PEGDA stoichiometric ratios: R_w = 1.9, 1.56, and 0.68% for M_n = 250 g mol^{-1}; 0.83, 0.68, and 0.29% for M_n = 575; and 0.68, 0.56, and 0.24% for M_n = 700 g mol^{-1} (see Figure 1d, isopleth line ②). These PI:PEGDA (w/w) ratios give molar ratios of 1:88, 1:107, and 1:248 (PI:PEGDA), respectively. Across all experiments (see Figure 2a–c and additional data available in SI Section S2), we find that increasing the PI:PEGDA (w/w) ratio results in decreased slope and z_f-intercept, corresponding to a simultaneous increase in both $\bar{\mu}$ (mm^{-1}) and K (cm^2 mJ^{-1}). Regardless of PEGDA M_n, $\bar{\mu}$ scales linearly with R_w, *viz.* $\bar{\mu}$ = 540.494 R + 0.12498 (Figure 2d). By contrast, while K also increases with the PI:PEGDA ratio (250 g mol^{-1}: 1.11 R_w, 575 g mol^{-1}: 2.21 R_w, and 700 g mol^{-1}: 3.04 R_w [cm^2 mJ^{-1}]), the rate of increases depends on the specific precursor M_n. The heat maps in Figure 2e–g summarize the interplay between the PI/PEGDA ratio and dose in terms of the resulting front position z_f. Corroborating our findings above, greater M_n leads to higher z_f at comparable d, for all PI:PEGDA (w/w) ratios. A crossover in front propagation kinetics, from faster to slower, is observed upon increasing PI concentration. This nonmonotonic effect with PI arises from the shifting balance between two governing parameters $\bar{\mu}$ and K: low PI leads to a higher d_c (and lower K), meaning that frontal propagation starts at later times (or higher doses), but it also leads to a lower $\bar{\mu}$ (optical attenuation) and thus faster front propagation. As a result, under low PI conditions, small variations in exposure dose d lead to significant changes in z_f, while under high PI conditions, z_f becomes less sensitive to d. This interplay highlights the importance of selecting appropriate PI concentrations and exposure d to optimize FPP processing (and associated economic and environmental trade-offs between PI loading and UV dose).

Unified K Values for Different M_n PEGDA

To understand why higher oligomer M_n results in faster polymerization kinetics, we consider instead the PI/PEGDA *molar ratio* ($R_m \equiv$ PI (mol)/PEGDA (mol)) across different formulations and compute the corresponding K and $\bar{\mu}$ values. We observe that K scales linearly with R_m (*viz.* K = 1.66 R_m [cm^2 mJ^{-1}]) irrespective of precursor M_n (Figure 2h). This suggests that the FPP rate constant is governed primarily by the stoichiometric ratio of reactive species, namely, PI molecules and acrylate end groups, rather than by the chain length of the oligomer (Figure 2i). These results also corroborate the notion that the K parameter derived from the coarse-grained FPP model represents an effective rate constant, which encapsulates the overall conversion dynamics at the macroscopic level. It should not be interpreted as an intrinsic molecular rate constant of the reaction but rather as a system-level parameter reflecting the solidification kinetics of the FPP formulation.

Modulating Pattern Curvature and Fluctuations with PEGDA Molecular Mass

We next consider the influence of PEGDA molecular mass on the self-assembly of FPP planar materials into 3D structures and their spatiotemporal response to environmental actuation. As outlined in Figure 3a, we fabricated and illustrated 2D starfish-shaped structures by UV patterning, subsequently

https://doi.org/10.1021/acs.macromol.5c02783
Macromolecules 2026, 59, 1978–1986

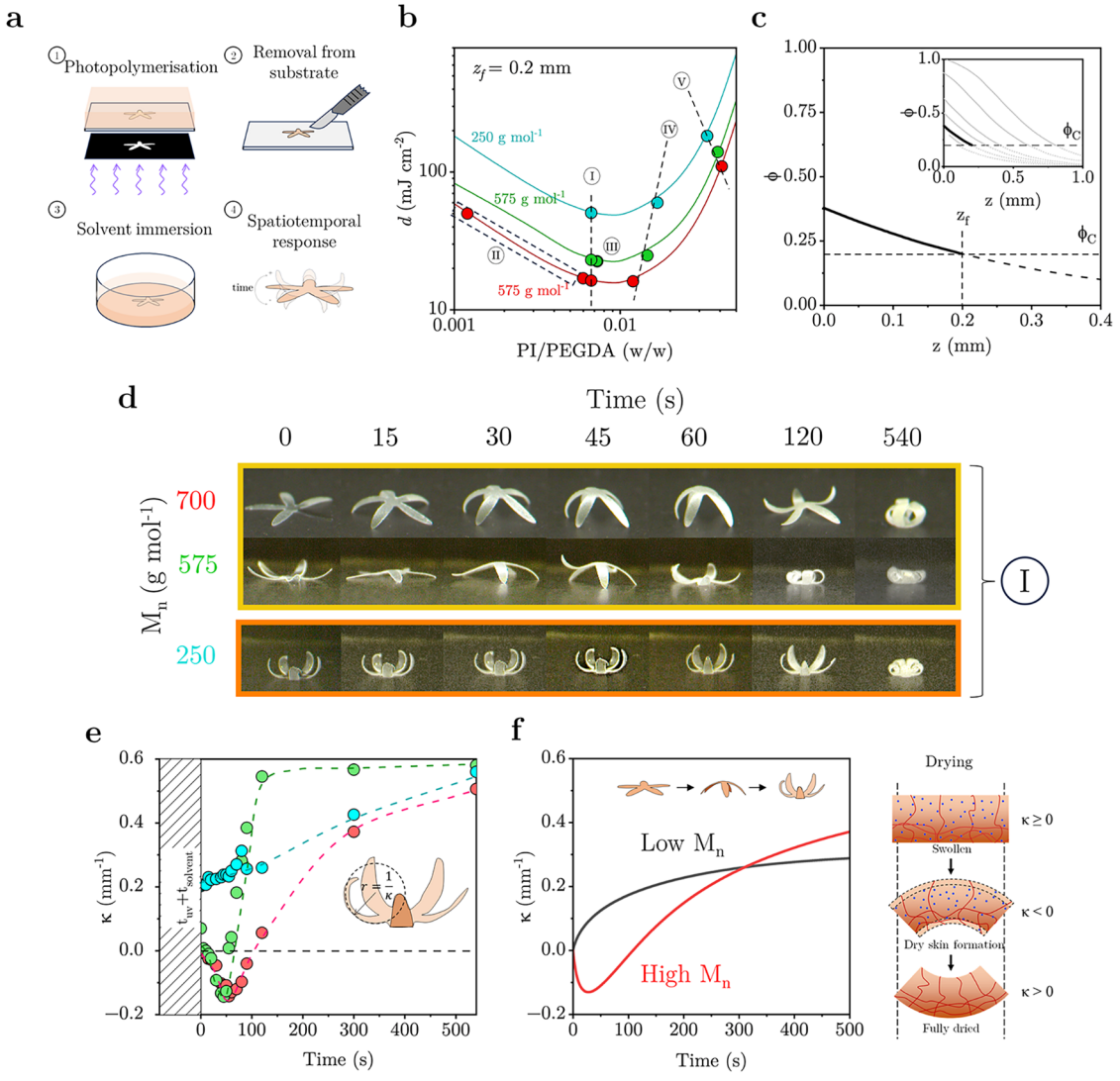

Figure 3. (a) Schematic of FPP fabrication and solvent development, depicting photopolymerization, substrate removal, solvent immersion, and spatiotemporal response. (b) Experimental map of PI/PEGDA (w/w) and irradiation dose d (mJ cm^{-2}) investigated, defining isopleths ① to ⑤, yielding a *constant* pattern thickness z_f = 0.2 mm. (c) FPP conversion $\phi(z)$ for isopleth ①, corresponding to constant PI/PEGDA (w/w) = 0.0067, and μ = 3.6 mm^{-1} at z_f = 0.2 mm. The inset illustrates $\phi(z, t)$ for higher irradiation doses, until full conversion of the skin layer. (d) Time-dependent 4D FPP structures obtained for a "starfish" pattern at isopleth ①, showing a nonlinear evolution of curvature κ. (e) Evolution of κ computed from images in (d). (f) Computed time-dependent κ profile and illustration of the fluctuation mechanism and associated drying of asymmetric FPP networks. Data for M_n 700 g mol^{-1} have been previously reported[33] and are included for comparison.

removed from their (glass) substrates, and immersed them into a developing solvent (ethanol) for 3 min. At the stage of solvent immersion, we observe the emergence of curvature ($\kappa \equiv 1/r$, where r is the radius of curvature) and monotonic or fluctuating profiles, which we find to depend on M_n. In this article, we define a minimal curvature fluctuation as the sequential transition $\kappa > 0 \rightarrow \kappa \leq 0 \rightarrow \kappa > 0$. The polymer network is then removed from ethanol and exposed to ambient conditions, where κ dynamics re-emerge.

We first examined a constant PI:PEGDA weight ratio of 0.67% (Figure 3b, isopleth line ①) to ensure the same $\bar{\mu}$. We fabricate starfish-shaped structures with different oligomers M_n and select d to achieve a constant $z_f \approx 0.2$ mm. These operating conditions ensure consistent $\phi(z)$ profiles, as depicted in Figure 3c.

Given that FPP innately yields asymmetric networks along the z-direction (normal to film surface), the spontaneous emergence of curvature can be expected due to a stress differential across the two facets, at $z = 0$ and $z = z_f$, due to the cross-linking gradient. In ambient air, the asymmetric networks fabricated from PEGDA with different M_n values exhibit a distinct spatiotemporal response (Figure 3d,e). Networks formed with M_n = 250 g mol^{-1} show a monotonic increase of curvature over time ($\kappa > 0$, bending toward low ϕ). However, networks fabricated from M_n = 575 and 700 g mol^{-1} display κ fluctuations in curvature during the drying process, from $\kappa \geq 0$ (nearly flat), to $\kappa < 0$ (bending toward high ϕ facet), and then back to $\kappa > 0$. These observations show that oligomer M_n plays a significant role in governing the structural dynamics and responsiveness of the printed material.

The origin of curvature fluctuations in photopolymerized PEGDA structures has previously discussed.[33] In short, these are caused by evaporation−diffusion of the solvent, which impacts the mechanical stress distribution evolution over time. Upon immediate exposure to ambient conditions, the swollen polymer begins to dry, rapidly forming a thin, stiff outer layer

https://doi.org/10.1021/acs.macromol.5c02783
Macromolecules 2026, 59, 1978−1986

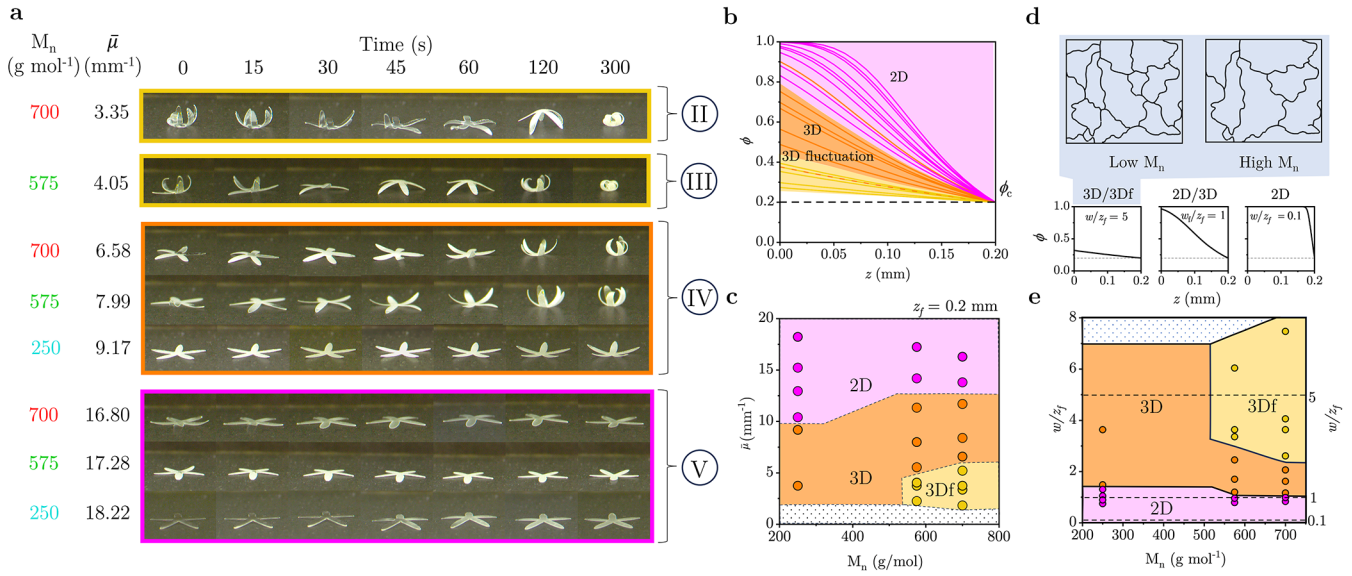

Figure 4. (a) 4D FPP origami "starfish" structures obtained with different oligomer M_n and $\bar{\mu}$, corresponding to isopleths ①-⑤ in Figure 3b (detailed in the SI). (b) Overlaid conversion profiles $\phi(z)$ corresponding to all isopleths ①-⑤ and SI Data S5, at constant z_f = 0.2 mm, color-coded according to the morphotemporal response: planar (purple), 3D structure (orange), 3D curvature fluctuation (yellow). The orange dashed line inside the yellow area indicates a system of M_n 250 g mol^{-1} that does not fluctuate. (c) Overall morphological response map of FPP origami in terms of M_n and $\bar{\mu}$. (d) Illustrative conversion profile $\phi(z)$ with various interfacial widths to pattern thickness ratios, w/z_f. The network schematics depict the cross-linking density of low- and high-molecular-weight oligomers (M_n), which dictates the 3D/3D curvature fluctuation behavior. (e) Morphological response map of FPP origami in terms of interfacial width w normalized with z_f and M_n.

due to surface evaporation. This dry skin induces interfacial stresses against the softer, solvent-rich interior, leading to an initial negative curvature. The effect is most pronounced when the base of the structure (more cross-linked) experiences greater compressive stress than the less cross-linked front interface. As drying progresses, the solvent diffuses outward from the interior, gradually increasing stiffness throughout the polymer. This redistribution of internal stress eventually reverses the curvature, resulting in a final positive bending as the system approaches equilibrium.

To explore this phenomenon, we employ a minimal modeling framework[33] based on the coupling of evaporation−diffusion phenomena according to Fick's second law and its boundary conditions at $z = 0$ (illuminated surface) and $z = z_f$ (solid−liquid interface) to compute the spatiotemporal profile of the solvent concentration along the polymer network

$$\frac{\partial C(z,t)}{\partial t} = \frac{\partial}{\partial z}\left(D_e \frac{\partial C(z,t)}{\partial z}\right) \tag{3}$$

where D_e is an "effective" diffusion constant, and t is the time following exposure to ambient air, imposing Robin boundary conditions

$$-D_e \frac{\partial C(z,t)}{\partial z}\bigg|_{z=0} = k_{evap}[C(0,t) - C_{air}] \tag{4}$$

$$-D_e \frac{\partial C(z,t)}{\partial z}\bigg|_{z=z_f} = -k_{evap}[C(z_f,t) - C_{air}] \tag{5}$$

for the rate of solvent loss at both interfaces, $z = 0$ and $z = z_f$ (analogous to common heat loss conditions due to convection at a surface).[38] We compare two representative cases of low and high PEGDA molecular masses, with simulation parameters summarized in SI Table S1. The high-M_n polymer network is capable of absorbing more solvent and undergoing greater swelling (see Figures S5 and S6), which we associate to its larger network mesh size. While $\phi(z)$ profiles are imposed to be constant in all M_n cases (ensured by identical $\bar{\mu}$ and ϕ_c values), the resulting mechanical response differs considerably. Building upon the model of Wang et al.,[39] we describe the evolution of the Young's modulus E during evaporation as

$$E(z,t) = E_0 + [E_{c,swollen}(\phi_c, \eta_{evap} = 0) + (E_{c,dry} - E_{c,swollen})(1 - \eta_{evap})^{n_1}][\phi - \phi_c]^{n_2} \tag{6}$$

where E_0 is the modulus of the neat network formed during photopolymerization upon reaching ϕ_c, E_c corresponds to the critical Young's modulus at fully dry ($\eta_{evap} = 0$) or swollen condition ($\eta_{evap} = 1$), and n_1 and n_2 correspond to the power law exponents for $\eta_{evap} = C(z,t)/C(z,t=0)$ and ϕ (within the range of 1.8−2.3, used as fitting parameters). Further, the curvature κ is quantified by computing the ratio of bending moment and bending stiffness as shown below

$$\kappa(t) = \frac{\int_0^{z_f} E(z,t)\varepsilon(z - z_N(t), t)\mathrm{d}z}{\int_0^{z_f} E(t)(z - z_N(t))^2 \mathrm{d}z} \tag{7}$$

where ε denotes strain and the position of the neutral axis z_N can be quantified as

$$z_N(t) = \frac{\int_0^h E(z,t) z \mathrm{d}z}{\int_0^h E(z,t)\mathrm{d}z} \tag{8}$$

This minimal model can capture the overall behavior (Figure 3f) observed in experiments and provides mechanistic insights into the M_n dependence of the curvature response. Details of simulation results are provided in Figure S9.

https://doi.org/10.1021/acs.macromol.5c02783
Macromolecules 2026, 59, 1978−1986

We rationalize the observations in terms of the higher cross-link density of lower precursor M_n networks, resulting in greater initial Young's modulus E_0 at the critical threshold ($\phi = \phi_c$) (see Figure S7). In turn, this increased stiffness reduces the mechanical contrast across the material interfaces, thus, reducing the internal stress gradient σ across the thickness. The generation of negative curvature can thus be expected to be reduced or suppressed in lower M_n structures, which aligns with our experimental observations of the absence of curvature fluctuation, contrasting with higher M_n counterparts (Figure 3f).

Unified Fabrication Framework for Nonplanar FPP Networks

We finally investigate the influence of varying $\bar{\mu}$ across three different oligomer precursor M_n at constant z_f = 0.2 mm, as shown in Figure 4a, with the PI:PEGDA (w/w) ratio based on Figure 3b, isopleth line (II)–(V), on spatiotemporal response of networks (additional data is available in Figure S8). In this series, we vary $\bar{\mu}$ via different PI:PEGDA ratios (w/w) and, to keep z_f constant, we adjust exposure dose d. Figure 4b shows the corresponding $\phi(z)$ profiles for all experiments shown in Figures 3d, 4a, and S5 (note that ϕ profiles for three different oligomer M_n with 0.67% PI:PEGDA w/w ratio overlap, hence the orange dashed line is provided to show different 3D/3D fluctuation outcome). In the network with higher oligomer M_n, when $\Delta\phi \equiv \phi(z = 0) - \phi(z_f = 0.2\ \text{mm})$ ($\approx$0.14–0.2), we observe 3D fluctuations. Outside of this range, regardless of M_n, the resulting structures are either flat (2D) when $\Delta\phi \approx 0.8$, or form 3D shapes without curvature fluctuation $\Delta\phi \approx 0.36$–0.55 or $\Delta\phi \approx 0.02$. However, for networks comprising low oligomer M_n, we found that across all $\Delta\phi$, the 3D flucuations are absent. Evidently, both $\bar{\mu}$ and network M_n dictate the dynamic response of FPP asymmetric networks, in terms of 2D, 3D, and 3D fluctuations at constant material thickness in the map depicted in Figure 4c (illustrated here for z_f = 0.2 mm). We observe that 3D structures exhibit curvature fluctuations emergence in high oligomer M_n (575 and 700 g mol^{-1}) within a limited range of $\bar{\mu} \approx 1.8$–$5.0\ \text{mm}^{-1}$. In other ranges of $\bar{\mu} \approx 5.0$–$12.0\ \text{mm}^{-1}$ and $\bar{\mu} \leq 1.5\ \text{mm}^{-1}$, the networks establish a 3D structure but do not show κ fluctuations. However, at $\bar{\mu} \geq 12.0\ \text{mm}^{-1}$, the networks do not assemble into a 3D structure (2D, $\kappa \leq 0.02\ \text{mm}^{-1}$). By contrast, networks with low oligomer M_n (250 g mol^{-1}) do not show any κ fluctuations within the experimental range of $\bar{\mu}$.

By adjusting $\bar{\mu}$, the mechanical properties across the network are altered according to the ϕ profile (Figure 4b). At high $\bar{\mu}$, where $\phi \gtrsim 0.8$ at $z = 0$ across all oligomer M_n, the Young's modulus E scales as a power of ϕ. This eventually increases the resistance to bend near $z = 0$, thereby suppressing curvature formation κ. For the emergence of 3D structures, the overall bending moment must be significant relative to resistance to bending.

Within the FPP framework, varying optical attenuation $\bar{\mu}$ governs the ϕ profile, and in turn, the interfacial width w, that is a metric for the steepness of the conversion gradient, as illustrated in Figure 4d. It is therefore tempting to compare the two length scales, w and z_f, and we thus obtain the morphological map in terms of a dimensionless interfacial width, w/z_f, shown in Figure 4e. This representation is analogous to that of Figure 4c but provides further clarity in that, for instance, 2D structures are found for $w/z_f \lesssim 1$, effectively when the interfacial width is commensurate or smaller than the pattern thickness (and therefore step-like conversion profiles). By contrast, 3D structures emerge for interfacial widths much broader than the pattern thickness, and thus smooth conversion profiles.

CONCLUSION

Our study demonstrates that oligomer molecular mass is a critical and easily tunable parameter in the design of 4D materials fabricated via frontal photopolymerization (FPP). By varying the chain length of a model difunctional acrylate oligomer, PEGDA, we isolated the influence of precursor M_n from FPP process conditions (optical attenuation and light exposure) to elucidate its impact on both polymerization kinetics and shape transformations.

Our findings show that while absolute polymerization kinetics vary with M_n, we find that the velocity of the propagating fronts are effectively unchanged but that higher M_n yields a lower critical threshold exposure and thus an earlier onset which results in faster kinetics at comparable time scales (or doses). These kinetics are governed primarily by the oligomer-to-photoinitiator ratio, indicating stoichiometric control over the front propagation behavior. However, the oligomer-to-photoinitiator ratio also dictates the competing relationship between K and $\bar{\mu}$, which results in a non-monotonic, albeit predictable, overall reaction rate. This insight provides a framework for the rational formulation design of FPP systems.

Moreover, we find that the solvent development of FPP networks can induce complex morphological responses, including curvature and fluctuating curvature, that also depend on M_n. Our minimal model of evaporation–diffusion coupled to the FPP equations can effectively capture the experimental observations and provide a useful design framework for FPP curvature dynamics. In general, higher M_n precursors yield networks with larger mesh dimensions (at constant thickness z_f) which support complex, nonmonotonic curvature evolution induced by solvent development. In contrast, lower molecular mass systems produce tighter networks that deform monotonically, as expected from the conversion (and stress) gradients across the thickness. Interfacial widths w larger than pattern thickness z_f are needed for the emergence of 3D behavior. Overall, our findings demonstrate how M_n can dictate the emergence, directionality and magnitude of pattern curvature κ, and its possible evolution in time. Our approach provides a facile design strategy for programming shape change into gradient polymer network materials without altering fabrication processes or external stimuli. When combined with the inherent gradient-forming capabilities of FPP, this approach offers a scalable, single-step route to structurally encoded 4D systems with potential applications in soft robotics, deployable biomedical scaffolds, adaptive optics, and beyond.

ASSOCIATED CONTENT

Supporting Information

The Supporting Information is available free of charge at https://pubs.acs.org/doi/10.1021/acs.macromol.5c02783.

FTIR for ϕ_c measurement; FPP model of traveling waves and additional kinetics data; solvent mass uptake for different PEGDA oligomer M_n; details of the simulation model, parameters, and results; and additional data on spatiotemporal responses on printed polymers (PDF)

https://doi.org/10.1021/acs.macromol.5c02783
Macromolecules 2026, 59, 1978–1986

AUTHOR INFORMATION

Corresponding Author

João T. Cabral − *Department of Chemical Engineering, Imperial College London, London SW7 2AZ, U.K.*; orcid.org/0000-0002-2590-225X; Email: j.cabral@imperial.ac.uk

Authors

Muhammad Ghifari Ridwan − *Department of Chemical Engineering, Imperial College London, London SW7 2AZ, U.K.*

Huseyin Mirac Dizman − *Department of Chemical Engineering, Imperial College London, London SW7 2AZ, U.K.; Department of Applied Science and Technology, Politecnico di Torino, Torino 10125, Italy;* orcid.org/0000-0001-5622-8440

Isobel Bentley − *Department of Chemical Engineering, Imperial College London, London SW7 2AZ, U.K.*

Alessandra Vitale − *Department of Applied Science and Technology, Politecnico di Torino, Torino 10125, Italy;* orcid.org/0000-0002-8682-3125

Complete contact information is available at: https://pubs.acs.org/10.1021/acs.macromol.5c02783

Notes

The authors declare no competing financial interest.

ACKNOWLEDGMENTS

We acknowledge funding from EPSRC (EP/X030938/1) and the EU Horizon 2021-2027 programme under the Marie Skłodowska-Curie Doctoral Networks (MSCA-DN) grant agreement No 101073432 (ESPERANTO). J.T.C. thanks the Royal Academy of Engineering (RCSRF1920/10/60) for funding a Research chair.

REFERENCES

(1) Kuang, X.; Roach, D. J.; Wu, J.; Hamel, C. M.; Ding, Z.; Wang, T.; Dunn, M. L.; Qi, H. J. Advances in 4D Printing: Materials and Applications. *Adv. Funct. Mater.* **2019**, *29*, No. 1805290.

(2) Fu, P.; Li, H.; Gong, J.; Fan, Z.; Smith, A. T.; Shen, K.; Khalfalla, T. O.; Huang, H.; Qian, X.; McCutcheon, J. R.; Sun, L. 4D printing of polymers: Techniques, materials, and prospects. *Prog. Polym. Sci.* **2022**, *126*, No. 101506.

(3) Naficy, S.; Gately, R.; Gorkin, R.; Xin, H.; Spinks, G. M. 4D Printing of Reversible Shape Morphing Hydrogel Structures. *Macromol. Mater. Eng.* **2017**, *302*, No. 1600212.

(4) Imrie, P.; Jin, J. Polymer 4D printing: Advanced shape-change and beyond. *J. Polym. Sci.* **2022**, *60*, 149−174.

(5) Nojoomi, A.; Jeon, J.; Yum, K. 2D material programming for 3D shaping. *Nat. Commun.* **2021**, *12*, No. 603.

(6) Xue, J.; Ge, Y.; Liu, Z.; Liu, Z.; Jiang, J.; Li, G. Photoprogrammable Moisture-Responsive Actuation of a Shape Memory Polymer Film. *ACS Appl. Mater. Interfaces* **2022**, *14*, 10836−10843.

(7) Li, Y.; Chen, H.; Liu, D.; Wang, W.; Liu, Y.; Zhou, S. pH-Responsive Shape Memory Poly(ethylene glycol)−Poly (ε-caprolactone)-based Polyurethane/Cellulose Nanocrystals Nanocomposite. *ACS Appl. Mater. Interfaces* **2015**, *7*, 12988−12999.

(8) Lendlein, A.; Jiang, H.; Jünger, O.; Langer, R. Light-induced shape-memory polymers. *Nature* **2005**, *434*, 879−882.

(9) Glugla, D. J.; Alim, M. D.; Byars, K. D.; Nair, D. P.; Bowman, C. N.; Maute, K. K.; McLeod, R. R. Rigid Origami via Optical Programming and Deferred Self-Folding of a Two-Stage Photopolymer. *ACS Appl. Mater. Interfaces* **2016**, *8*, 29658−29667.

(10) Kotikian, A.; Watkins, A. A.; Bordiga, G.; Spielberg, A.; Davidson, Z. S.; Bertoldi, K.; Lewis, J. A. Liquid Crystal Elastomer Lattices with Thermally Programmable Deformation via Multi-Material 3D Printing. *Adv. Mater.* **2024**, *36*, No. 2310743.

(11) Dudek, K. K.; Kadic, M.; Coulais, C.; Bertoldi, K. Shape-morphing metamaterials. *Nat. Rev. Mater.* **2025**, *10*, 783−798.

(12) Meeussen, A. S.; Corvi, A.; Bertoldi, K. A New Design Strategy for Highly Multistable Kirigami Metamaterials. *Adv. Funct. Mater.* **2025**, *35*, No. 2421638.

(13) Zhao, Z.; Wu, J.; Mu, X.; Chen, H.; Qi, H. J.; Fang, D. Origami by frontal photopolymerization. *Sci. Adv.* **2017**, *3*, No. e1602326.

(14) Liu, Y.; Boyles, J. K.; Genzer, J.; Dickey, M. D. Self-folding of polymer sheets using local light absorption. *Soft Matter* **2012**, *8*, 1764−1769.

(15) Ware, T. H.; Perry, Z. P.; Middleton, C. M.; Iacono, S. T.; White, T. J. Programmable Liquid Crystal Elastomers Prepared by Thiol−Ene Photopolymerization. *ACS Macro Lett.* **2015**, *4*, 942−946.

(16) Holmes, D. P.; Roché, M.; Sinha, T.; Stone, H. A. Bending and twisting of soft materials by non-homogenous swelling. *Soft Matter* **2011**, *7*, 5188.

(17) Janbaz, S.; Hedayati, R.; Zadpoor, A. A. Programming the shape-shifting of flat soft matter: from self-rolling/self-twisting materials to self-folding origami. *Mater. Horiz.* **2016**, *3*, 536−547.

(18) López-Díaz, A.; Martín-Pacheco, A.; Rodríguez, A. M.; Herrero, M. A.; Vázquez, A. S.; Vázquez, E. Concentration Gradient-Based Soft Robotics: Hydrogels Out of Water. *Adv. Funct. Mater.* **2020**, *30*, No. 2004417.

(19) Cheng, Y.; Ren, K.; Yang, D.; Wei, J. Bilayer-type fluorescence hydrogels with intelligent response serve as temperature/pH driven soft actuators. *Sens. Actuators, B* **2018**, *255*, 3117−3126.

(20) Liu, H.; Liu, R.; Chen, K.; Liu, Y.; Zhao, Y.; Cui, X.; Tian, Y. Bioinspired gradient structured soft actuators: From fabrication to application. *Chem. Eng. J.* **2023**, *461*, No. 141966.

(21) Cabral, J. T.; Hudson, S. D.; Harrison, C.; Douglas, J. F. Frontal Photopolymerization for Microfluidic Applications. *Langmuir* **2004**, *20*, 10020−10029.

(22) Vitale, A.; Hennessy, M. G.; Matar, O. K.; Cabral, J. T. Interfacial Profile and Propagation of Frontal Photopolymerization Waves. *Macromolecules* **2015**, *48*, 198−205.

(23) Vitale, A.; Hennessy, M. G.; Matar, O. K.; Cabral, J. T. A Unified Approach for Patterning via Frontal Photopolymerization. *Adv. Mater.* **2015**, *27*, 6118−6124.

(24) Cabral, J. T.; Douglas, J. F. Propagating waves of network formation induced by light. *Polymer* **2005**, *46*, 4230−4241.

(25) Hennessy, M. G.; Vitale, A.; Matar, O. K.; Cabral, J. T. Controlling frontal photopolymerization with optical attenuation and mass diffusion. *Phys. Rev. E* **2015**, *91*, No. 062402.

(26) Hennessy, M. G.; Vitale, A.; Cabral, J. T.; Matar, O. K. Role of heat generation and thermal diffusion during frontal photopolymerization. *Phys. Rev. E* **2015**, *92*, No. 022403.

(27) Zhao, Z.; Wu, J.; Mu, X.; Chen, H.; Qi, H. J.; Fang, D. Desolvation Induced Origami of Photocurable Polymers by Digit Light Processing. *Macromol. Rapid Commun.* **2017**, *38*, No. 1600625.

(28) Wang, J.; Dai, N.; Jiang, C.; Mu, X.; Zhang, B.; Ge, Q.; Wang, D. Programmable shape-shifting 3D structures via frontal photopolymerization. *Mater. Des.* **2021**, *198*, No. 109381.

(29) Brown, W. H. The Mechanism of Movement and the Duration of the Effect of Stimulation in the Leaves of Dionaea. *Am. J. Bot.* **1916**, *3*, 68−90.

(30) Harrington, M. J.; Razghandi, K.; Ditsch, F.; Guiducci, L.; Rueggeberg, M.; Dunlop, J. W.; Fratzl, P.; Neinhuis, C.; Burgert, I. Origami-like unfolding of hydro-actuated ice plant seed capsules. *Nat. Commun.* **2011**, *2*, No. 337.

(31) Vandenbrink, J. P.; Brown, R. I.; Harmer, S. L.; Blackman, B. K. Turning heads: The biology of solar tracking in sunflower. *Plant Sci.* **2014**, *224*, 20−26.

(32) Kuang, X.; Wu, J.; Chen, K.; Zhao, Z.; Ding, Z.; Hu, F.; Fang, D.; Qi, H. J. Grayscale digital light processing 3D printing for highly functionally graded materials. *Sci. Adv.* **2019**, *5*, No. 5790.

(33) Ridwan, M. G.; Ahmad, Z.; Vitale, A.; Cabral, J. T. Fluctuating Curvature and Actuation in 4D Printed Asymmetric Networks by Frontal Photopolymerization. *Adv. Mater. Interfaces* **2026**, No. e00879.
(34) Zhang, H.; Wang, L.; Song, L.; Niu, G.; Cao, H.; Wang, G.; Yang, H.; Zhu, S. Controllable properties and microstructure of hydrogels based on crosslinked poly(ethylene glycol) diacrylates with different molecular weights. *J. Appl. Polym. Sci.* **2011**, *121*, 531−540.
(35) Warren, J.; Cabral, J.; Douglas, J. Solution of a field theory model of frontal photopolymerization. *Phys. Rev. E* **2005**, *72*, No. 021801.
(36) Hennessy, M. G.; Vitale, A.; Matar, O. K.; Cabral, J. T. Monomer diffusion into static and evolving polymer networks during frontal photopolymerisation. *Soft Matter* **2017**, *13*, 9199−9210.
(37) Purnama, A. R.; Hennessy, M. G.; Vitale, A.; Cabral, J. T. Coarse-grained models for frontal photopolymerization with evolving conversion profile. *Polym. Int.* **2017**, *66*, 752−760.
(38) Incropera, F. P.; DeWitt, D. P.; Bergman, T. L.; Lavine, A. S. *Fundamentals of Heat and Mass Transfer*; John Wiley & Sons, Inc.: New York, 1990; Vol. *1072*.
(39) Wang, J.; Mu, X.; Li, D.; Yu, C.; Cheng, X.; Dai, N. Modeling and Application of Planar-to-3D Structures via Optically Programmed Frontal Photopolymerization. *Adv. Eng. Mater.* **2019**, *21*, No. 1801279.

https://doi.org/10.1021/acs.macromol.5c02783
Macromolecules 2026, 59, 1978−1986